Research Square

Preprints are preliminary reports that have not undergone peer review.
They should not be considered conclusive, used to inform clinical practice,
or referenced by the media as validated information.

Programmable spinning of integrated circuit fibers

Gang Wang

gwf8707@dhu.edu.cn

Donghua University

Fengqiang Sun

Donghua University

Fen Jiang

Donghua University

Kaige Wang

Donghua University

Weichu Chen

Donghua University

Futeng Liu

Donghua University

Yida Hong

Donghua University

Xingbo Han

Donghua University

Mingbo Zhao

Donghua University

Yuwen Zhu

Donghua University

Hengda Sun

Donghua University https://orcid.org/0000-0003-3164-4557

Hongzhi Wang

Donghua University https://orcid.org/0000-0002-5469-2327

Meifang Zhu

Donghua University https://orcid.org/0000-0003-0359-3633

Article

Keywords:

Posted Date: November 7th, 2025

DOI: https://doi.org/10.21203/rs.3.rs-7818608/v1

License: This work is licensed under a Creative Commons Attribution 4.0 International License.
Read Full License

Additional Declarations: There is **NO** Competing Interest.

Programmable spinning of integrated circuit fibers

Fengqiang Sun[1], Fen Jiang[1], Kaige Wang[1], Weichu Chen[1], Futeng·Liu[2], Yida Hong[1], Xingbo Han[1], Mingbo Zhao[2], Yuwen Zhu[1], Hengda Sun[1]*, Hongzhi Wang[1], Meifang Zhu[1], Gang Wang[1]*

[1]State Key Laboratory of Advanced Fiber Materials, College of Materials Science and Engineering, Donghua University, Shanghai 201620, P. R. of China.

[2]College of Information Science and Technology, Donghua University, Shanghai 201620, P. R. of China.

*Corresponding author. Email: sunhengda@dhu.edu.cn, gwf8707@dhu.edu.cn.

Abstract

Embedding circuit-level functionality directly into fibers would fundamentally reconfigure how we construct, integrate, and wear intelligent systems. Here, we report a scalable microfluidic encoding strategy to fabricate integrated circuit fibers (IC fibers) that support multiple essential electronic functions within a continuous, deformable architecture. By dynamically encoding modular functional layers within each fiber, we fabricate four distinct types of integrated circuit (IC) fibers, each emulating a core electronic function: electroluminescent IC (EL-IC) fibers for light emission, resistor and capacitor IC (RC-IC) fibers for analog signal processing, organic electrochemical transistors IC (OECT-IC) fibers for digital logic operations, and electroquasistatic IC (EQS-IC) fibers for wireless, contactless sensing and control. In a departure from conventional methods that embed discrete devices, our approach redefines the fiber itself as the active circuit element. We demonstrate that the fibers can be woven, sewn, or arranged into textiles capable of full-color displays, real-time analog filtering, logic gating, free-space spatial tracking, and remote robotic control. This fiber-as-circuit architecture offers a foundational platform for reimagining textiles not as passive substrates, but as active computing media.

Main

Traditional artificial intelligence emphasizes centralized processing power, which faces limitations in real-world applications that require context, sensory feedback, and adaptability.[1,2] In contrast, embodied intelligence highlights cognition emerging from the interaction of body, environment, and controller. This requires tight integration of sensing, actuation, and computation at the material level.[3–5]

Flexible and wearable electronics represent an ideal physical platform for realizing such embodied intelligence, yet their hardware implementation faces significant challenges.[6,7] Most current systems rely on rigid chips bonded to soft substrates, limiting adaptability and decoupling sensing from processing.[8,9] While electronic textiles offer integration of sensing, processing, and feedback in a single medium,[10–12] existing methods often suffer from poor fiber utilization and unstable interconnects. Embedding multiple functions in a single fiber is a promising solution, pursued via two main strategies: thermal drawing[13–15] and photolithography.[16,17] However, thermal drawing requires heat-tolerant, miniaturized components and complex preforms, while photolithography is constrained by the need for heat-resistant, smooth fibers, limiting materials and scalability.[18]

In this context, we present a microfluidic spinning approach[19–21] to create IC fibers with modular, functional layers. Guided by precise circuit design and microfluidic control of fiber formation, we combine a conductive layer with various functional layers to form unique modules capable of electron-photon,[22] electron-electron,[23] and electron-ion[24] carrier conversion, and EQS modulation.[25] By further arranging and integrating these modules during microfluidic spinning, we can yield customizable circuits within a single fiber, significantly enhancing both stability and fiber utilization **(Fig. 1a)**. In this "fiber-as-circuit" architecture, the fibers are no longer passive substrates for discrete components but are themselves the active computational elements. This approach bridges flexibility and computational capacity, enabling fibers that can sense, process, and respond in real time. Here, we have customized four types of IC fibers: EL-IC fibers for colorful light-emitting based on electron-photon conversion **(Fig. 1b,**

Fig. 3), RC-IC fibers for analog signal processing leveraging electron-electron conversion **(Fig. 1c, Fig. 4)**, OECT-IC fibers for digital signal processing relying on electron-ion conversion **(Fig. 1d,** Error! Reference source not found.**)**, and EQS-IC fibers for touchless sensing based on the principles of EQS field modulation and capacitive coupling sensing **(Fig. 1e,** Error! Reference source not found.**)**.

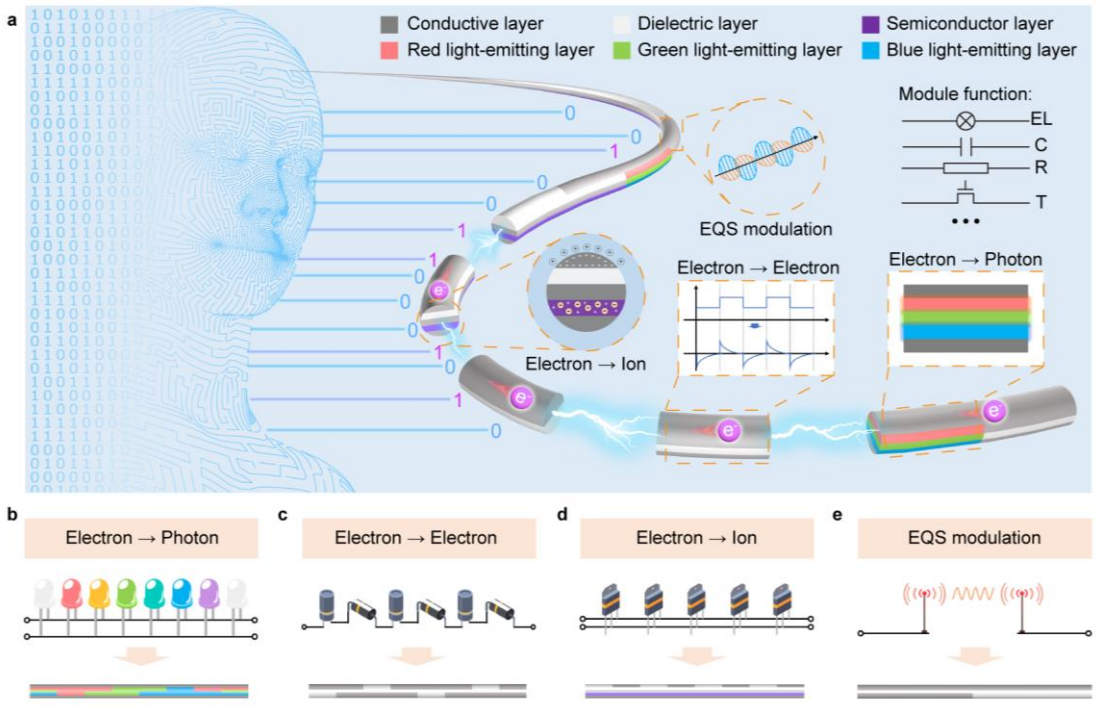


Fig. 1. Design and principle of the IC fibers. a. Conceptual image of IC fibers for embodied intelligence. **b.** An electron-photon fiber circuit equivalent to multiple multi-color light bulbs in parallel. **c.** An electron-electron fiber circuit equivalent to capacitors and resistors connects in alternating series. **d.** An electron-ion fiber circuit equivalent to multiple OECT devices in parallel. **e.** An EQS modulation fiber circuit equivalent to a transmitter–receiver pair.

IC Fiber Fabrication Process and Fluid Encoding Simulations

Integrating multiple devices within an IC fiber requires precise control over both device structure and interconnections. This is achieved by dynamically encoding connected and disconnected regions using microfluidic spinning. We designed a chip with five input channels (**Supplementary Fig. 2**), each controlled by an independent pneumatic pump (#1~#5, **Supplementary Fig. 1**), allowing for flexible precise flow control and

flow encoding **(Fig. 2a**, various encoding methods were tested in **Supplementary Fig. 3-7)**. Thermoplastic polyurethane (TPU) was chosen as the polymer matrix for the entire IC fiber, with different functional materials added to create various functional layers. This approach maximizes the fiber's ability to cure and form while maintaining the stability of the interlayer interfaces. The inset in the upper-right corner of **Fig. 2a** illustrates the three stages of fiber formation: the amorphous stage, the molecular chain orientation stage, and the curing stage.

The spinning process involves constant and variable flows. We focus on EL-IC fibers as a representative case to simulate structural formation and interface diffusion. Five labeled flows (A-E) form conductive layers (A, E; constant) and RGB-emitting layers (B, C, D; variable). Differences in viscosity and density among solutions lead to interface shaping **(Supplementary Fig. 8)**, as detailed in **Methods**.

Under constant flow, the five-layer stream converges in parallel. Viscosity differences and wall friction induce pressure gradients, curving the fluid interfaces downstream **(Fig. 2b)**. As a result, the fluid layers gradually change from a parallel structure at the inlet (b_1) to a curved shape (b_3). From b_3 to the channel outlet (b_5), where the channel width no longer changes, the arc-shaped structural variation due to interlayer diffusion occurs more slowly.

Diffusion between adjacent layers is characterized by the Péclet number (*Pe*), which compares convection and diffusion **(Fig. 2c)**. High *Pe* values indicate dominance of convection, preserving interface sharpness. The *Pe* formula and theoretical derivation are provided in **Methods**.[26] To minimize diffusion, the channel length L was set much shorter than the calculated diffusion length l, ensuring well-defined interfaces between functional layers.

Dynamic flow coding enables modular separation and integration. The flow rate curve in **Fig. 2d** shows the precise switching capability of each channel between defined flow rates of 50 μL min^{-1} (on state) and zero (off state). The switching of flow rate encoding is instantaneous, but the transition between fluid states is not instantaneous. Under laminar flow conditions, the pressure-driven flow inside the square channel producing parabolic velocity profiles typical of Poiseuille flow. In this profile, the fluid

in the center moves faster than the fluid near the edges. To simulate this phenomenon, a steady-state multiphase flow model was used in Fluent **(Fig. 2e)**, with the fluid encoding sequence matching the flow rate waveforms shown in **Fig. 2d**.

During each transition, Taylor dispersion occurs due to velocity gradients across the channel cross-section. This dispersion introduces a transient mixing effect, which can compromise the clarity of fluid interfaces. The effective diffusion coefficient (D_{eff}) in a rectangular channel is expressed as:

$$D_{eff} = D[1 + \frac{1}{210}(\frac{vh}{D})^2] \quad (1)$$

where h is the layer height (m), and f is the shape factor, which increases with the aspect ratio (W/h) of the layer. According to the formula, reducing the average flow velocity of the spinning solutions mitigates the effects of Taylor dispersion, preserving sharp fluid interfaces. The length of the trailing fluid (fluid tail) after switching depends on channel size. Sufficient encoding duration is required to ensure layer clarity. Furthermore, miniaturizing the chip improves spatial resolution.

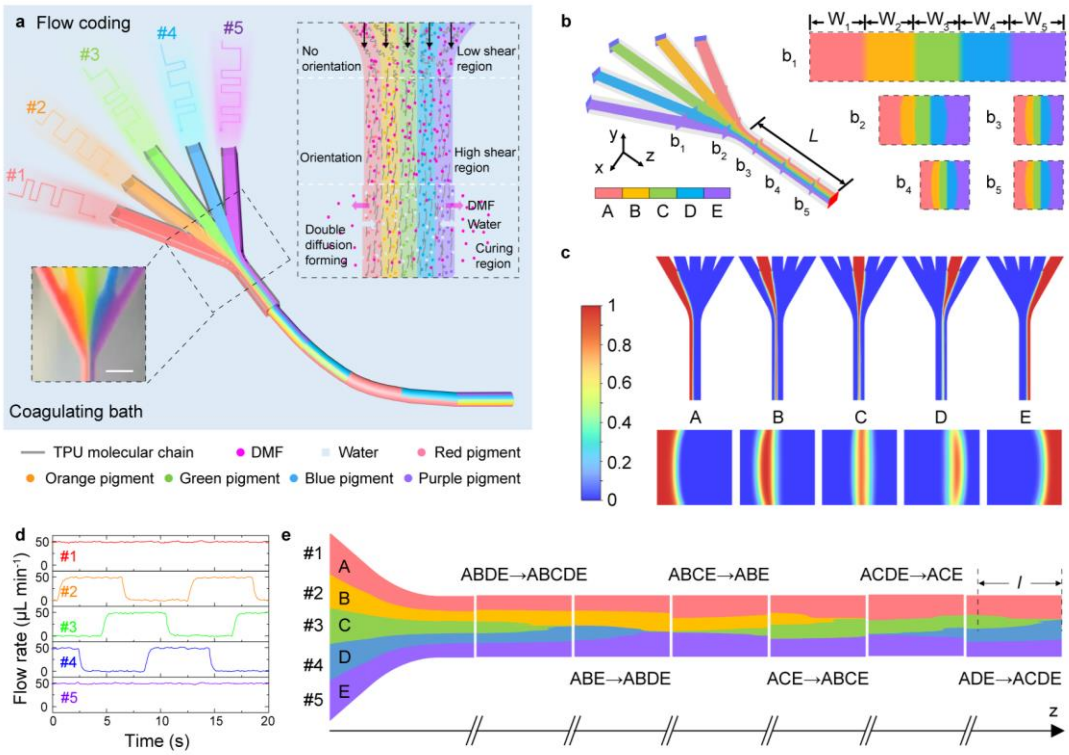


Fig. 2. IC fiber fabrication process and fluid encoding simulations. a. Schematic of fluid encoding microfluidic spinning. The left inset shows a photo of the intersection of five flow channels. Scale bar: 1 mm. The right inset illustrates the three stages of fiber

formation during the microfluidic spinning process: molecular chain non-orientation, molecular chain orientation, and solvent double-diffusion fiber curing. Simulations of fluid layer diffusion under constant flow conditions (**b**) and interlayer interface diffusion (**c**). The flow rate switching encoding curve for the five flow channels (**d**) and its corresponding fluid state switching simulation (**e**).

EL-IC Fibers for Electron-Photon Conversion

To demonstrate electron-photon conversion, we designed EL-IC fibers with RGB light-emitting modules arranged in parallel, mimicking multicolor LED circuits **(Fig. 1b)**. Each fiber features a sandwich structure with RGB electroluminescent layers (ZnS:Cu/TPU + pigments) between two conductive Ag/TPU layers (details of conductivity parameters in **Supplementary Fig. 9**). The modular structure is programmable via fluid encoding, supporting both precise switching encoding **(Fig. 3a)** and waveform encoding **(Fig. 3d)**.

RGB layers can be encoded through alternating (R, G, and B), binary (R+G, G+B, and B+R), or ternary (R+G+B) stacking to produce a broad color spectrum (**Fig. 3a**, **Supplementary Fig. 10d)**. Following spectral sequence, switching the RGB flows yields layered color outputs like red, green, blue, orange, cyan, purple, and white. The flow rates for switching coding range from 0 to 50 μL min^{-1} (with conductive layers fixed at 30 μL min^{-1}) and switching intervals of 5 s (**Fig. 3b**). Due to fluid tailing, transitions are gradual (**Fig. 3c**). Cross-sectional fluorescence imaging shows distinct layered aligned between conductive electrodes (**Supplementary Fig. 11**). Due to identical base materials, SEM-EDS confirms seamless between Ag layers and the RGB layers (**Supplementary Fig. 12**), which enhance functional stability. Beyond switching, waveform encoding enables continuous color gradients (**Fig. 3d-f**).

Emission color depends on RGB layer thickness, tunable via flow rate control. CIE chromaticity coordinate (**Fig. 3g and Supplementary Video 2**) confirms this modular design enables the generation of any color within the triangle (R, G, and B as vertices), allowing a wide and versatile electroluminescent color spectrum. For instance, EL-IC fibers with electroluminescent layers of equal thickness for two colors have their CIE

coordinates at the midpoints of the triangle's edges, while fibers with equal thicknesses of all three colors are located at the triangle's center. Achieving this degree of precise and diverse color modulation within a single fiber is unprecedented in traditional fiber technologies.

EL-IC fibers offer tunable luminance under varying voltage and frequency (**Supplementary Fig. 12a**). When the electric field increased from 1 V μm^{-1} to 2 V μm^{-1}, the luminance of R, G, and B fibers significantly rose from 0.1 cd m^{-2} each to 21.3 cd m^{-2}. Furthermore, luminance was measured for RGB EL-IC fibers at rotation angles from 0° to 360° in 15° increments and mapped onto a polar coordinate system **(Supplementary Fig. 12b)**. Peak brightness aligns with 0°/180° fiber orientation, while minima at 90°/270° arise from conductive layer shielding, indicating anisotropic emission. Such angle-dependent behavior is directly linked to the fiber's layered internal structure.

EL-IC fibers maintain structural integrity or functionality through sewing and weaving processes due to excellent flexibility and mechanical strength (**Supplementary Fig. 12c**). They were used to create full-color embroidery patterns of Donghua University (**Fig. 3h**) and woven into textile displays using conventional looms (**Fig. 3i**), validating their structural robustness and design versatility. These examples vividly demonstrate the feasibility of the modular integration strategy in creating highly versatile and customisable integrated circuits within a single fiber.

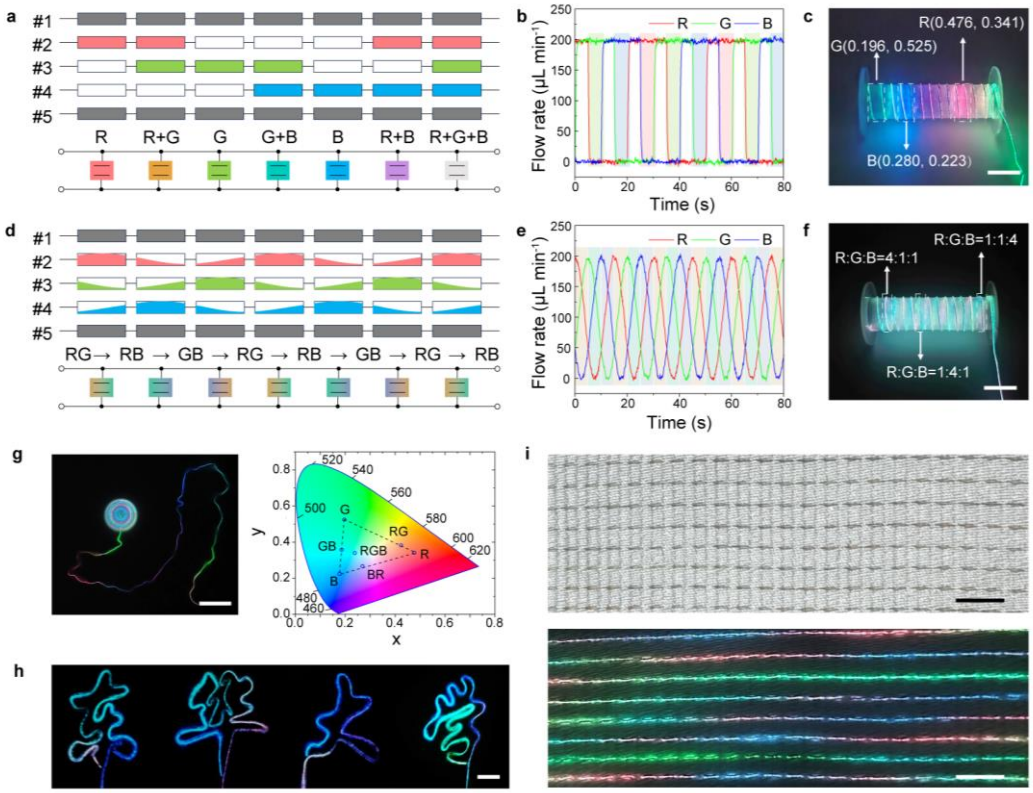


Fig. 3. EL-IC fibers for electron-photon conversion. a. Modular structure of the light-emitting colors encoding via fluid switching and the corresponding equivalent circuit. **b.** Curve illustrating RGB layer encoding via fluid switching and (**c**) corresponding electroluminescent fiber image. **d.** Modular structure of the light-emitting colors encoding via fluid waveform modulation and the corresponding equivalent circuit. **e.** Curve illustrating RGB layer encoding via fluid waveform modulation and (**f**) corresponding electroluminescent fiber image. **g.** Photographic image and CIE chromaticity coordinates of different light-emitting modules. **h.** Patterned embroidery created with EL-IC fibers. **i.** Full-color electroluminescent fabric. Scale bar: **c.** 1 cm, **f.** 1 cm, **g.** 10 cm, **h.** 1 cm, **i.** 1 cm.

RC-IC Fibers for Electron-Electron Conversion

The electron-electron conversion capability of IC fibers is primarily manifested through the transformation of analog signals. To implement analog signal processing within fibers, we developed RC-IC fibers that integrate resistive (R) and capacitive (C) elements. In this design, Conductive layers (Ag/TPU) are formed via channels #1 and

#5, while dielectric layers ($BaTiO_3$/TPU) are introduced via channels #2, #3, and #4. By adjusting flow codes, we fabricated RC-IC fibers with either parallel (**Fig. 4a**) or series (**Fig. 4e**) circuit configurations.

The performance of the RC-IC fibers is dictated by the resistance (R) and capacitance (C) values. We test included measuring the thickness of the layered structure in a 1 cm section of the fiber at different flow rates (**Supplementary Fig. 13, SEM**). By tailoring the unit resistance and capacitance, we can precisely design RC circuits for specific applications.

For RC parallel circuits, both DC and AC signals can pass through. A first-order RC circuit features a cut-off frequency (f_0) defined as:

$$f_0 = \frac{1}{2\pi RC} \tag{2}$$

When the input signal frequency is lower than f_0, the circuit behaves as a DC circuit with a total impedance equal to R. When the frequency exceeds f_0, the capacitive reactance becomes negligible, and the total impedance approaches zero as the frequency increases. In contrast, RC series circuits block DC signals due to the capacitor, and both R and C contribute to the total impedance, which varies with frequency. For input signal frequencies greater than f_0, the total impedance stabilises and equals R.

Real RC-IC fibers include electrode resistance (R_e) and dielectric losses, introducing equivalent series resistance (ESR). This shifts the cutoff frequency slightly lower than ideal, altering the cutoff frequency to:

$$f_0 = \frac{1}{2\pi(R+R_e)C} \tag{3}$$

RC-IC fibers represent a type of analogue circuit with a wide range of practical functionalities, including integration, differentiation, coupling, and filtering. In first-order RC circuits, when the time constant $\tau=(R+R_e)C$ is significantly larger than the input waveform's width T_w ($\tau \gg T_w$), the fiber acts as an integrator. In this configuration, the RC series circuit connects U_{in} to the input, with the capacitor C serving as the output U_{out}. The equivalent circuit and wiring are shown in **Fig. 4b**.

Fig. 4c demonstrates the integration function of an RC-IC fiber, where R = ~8.46 kΩ, R_e = ~75.5 Ω, and C = ~18.2 pF. Under a 1 V_{pp}, 800 kHz square wave input, the

integrator transforms the input into a sawtooth waveform. The waveforms corresponding to different frequencies are shown in **Supplementary Fig. 14**. The fiber also acts as a low-pass filter, attenuating signals above ~1.02 MHz, as demonstrated by Bode plot measurements (**Fig. 4d**).

Similarly, when $\tau \ll T_w$, the RC-IC fiber acts as a differentiator. In this case, R connects to the output U_{out}, while C is at the input, as shown in **Fig. 4f**. **Fig. 4g** illustrates the differentiation function, where R = 13.01 kΩ, R_e = 27.4 Ω, and C = 12.8 pF. This configuration transforms a 1 V_{pp}, 600 Hz square wave into alternating positive and negative spikes, corresponding to the rising and falling edges of the input waveform. The waveforms corresponding to different frequencies are shown in **Supplementary Fig. 15**. Frequency response tests confirm high-pass filtering behavior, with a -3 dB point at ~995 kHz (**Fig. 4h**).

OECT-IC Fibers for Electron-Ion Conversion

While RC-IC fibers, as analogue circuits, demonstrate the ability to continuously modulate dynamic signals through resistor-capacitor coupling, logic circuits focusing on discrete digital signals play a critical role in modern electronic systems.[27] To realize such functionalities in fiber form, we developed OECT-IC fibers by integrating multiple OECT modules—devices capable of modulating electron-ion transport. This approach allowed the integration of multiple OECTs within a single fiber, imparting distributed logic capabilities and multi-channel signal processing functionality.

Each OECT module features five layers: layer 1: gate electrode (Ag/AgCl paste/TPU), layer 2: insulating layer ($BaTiO_3$/TPU), layer 3 and 5: source and drain electrodes (Ag paste/TPU), layer 4: semiconductor layer (p(g2T-T)/TPU). The gate layer is periodically encoded while others are continuously spun (**Fig. 4i**). This encoding strategy enables the integration of multiple independent OECT units (G_1, G_2, G_3, …, G_n) along a single fiber (**Fig. 4j**). The equivalent circuit of the fiber can thus be regarded as a parallel structure of OECTs, each independently controlled by its respective gate electrode (**Fig. 4i**).

The physical structure of a single OECT-IC fiber is shown in **Fig. 4j** and **Supplementary Fig. 16**, revealing clear stratification of the fiber. The transfer and output characteristics tests using an ionic liquid 1-Ethyl-3-Methylimidazolium bis(triFluoroMethylSulfonyl)Imide ([EMIM][TFSI]) electrolyte demonstrate enhancement-mode OECT behavior, with a maximum on-state current of 0.6 mA and peak transconductance of 1.09 mS (**Fig. 4k, l**). The semiconductor layer (~150 μm thick) forms the active channel, while the porous fiber matrix facilitates ion infiltration and efficient doping, enabling modulation of source-drain conductivity via ionic gating.

Interconnecting source and drain lines while independently addressing each gate enables logic operations. For example, when both V_{G1} and V_{G2} = 0 V, the channels conduct (logic "0"); if either gate is -0.2 V, output current drops (logic "1"). This demonstrates OR logic behavior embedded directly in the fiber **(Fig. 4m** and **Supplementary Fig. 17)**.

Sequential gating of OECTs (G_1~G_3) using -0.7 V steps yields a staircase increase in the total drain current $-I_{out}$ (**Fig. 4n** and **Supplementary Fig. 18**). This multilevel activation enables digital-to-analog conversion and tiered logic processing, showcasing OECT-IC fibers' scalability and potential for complex in-fiber logic networks.

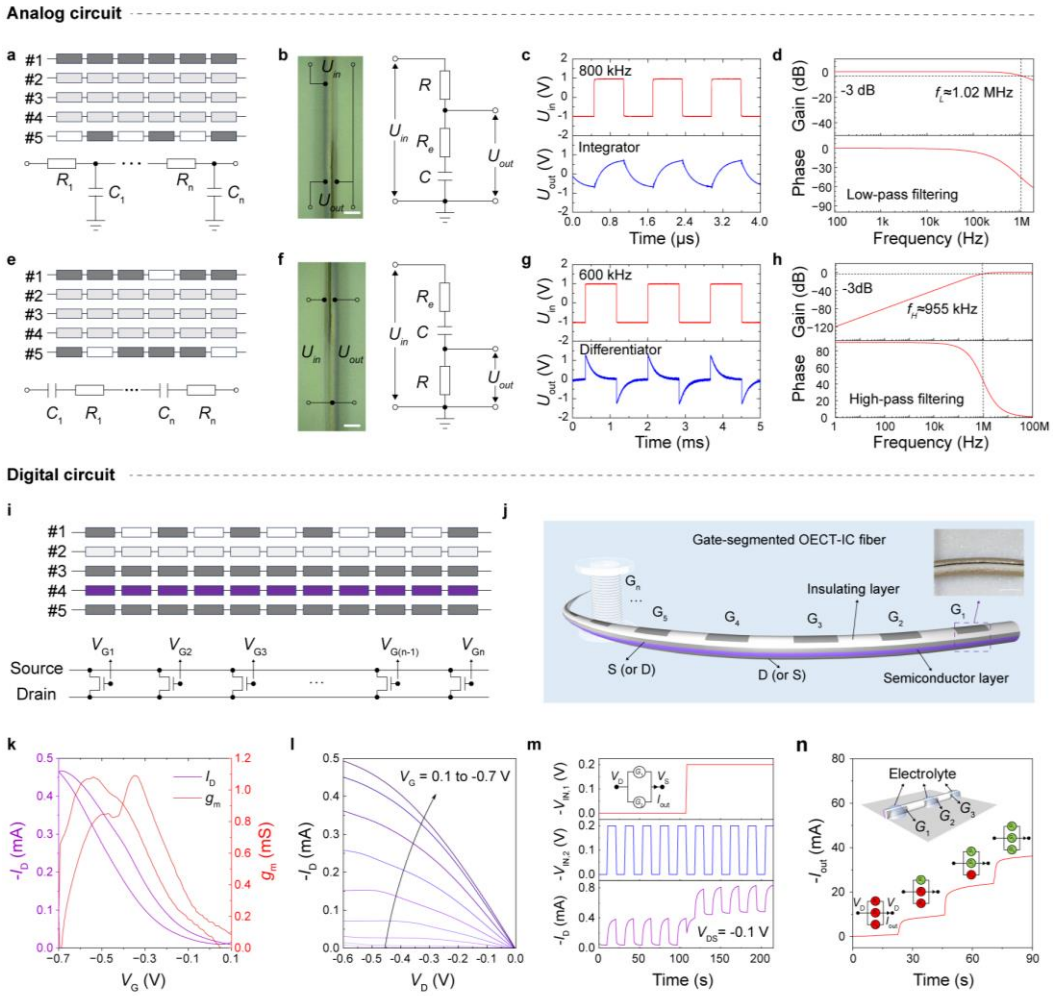


Fig. 4. RC-IC fibers for electron-electron conversion and OECT-IC fibers for electron-ion conversion: (a) Microfluidic coding method and equivalent circuit of RC parallel circuit fiber. (b) Photograph, connection mode and equivalent circuit of first-order RC circuit fiber for integrator circuit. Scale bar: 1 mm. (c) The performance of RC integral circuit fiber under 1 V_{pp}, 800 kHz. (d) The bode diagram of RC low-pass circuit. (e) Microfluidic coding method and equivalent circuit of RC series circuit fiber. (f) Photograph, connection mode and equivalent circuit of first-order RC circuit fiber for differential circuit. Scale bar: 1 mm. (g) The performance of RC differential circuit fiber under 1 V_{pp}, 600 Hz. (h) The bode diagram of RC high-pass circuit. (i) Microfluidic coding method and equivalent circuit of gate-segmented OECT-IC fiber. (j) Schematic diagram of gate-segmented OECT fiber and photos of a single OECT segments module. Scale bar:1 mm. (k) Transfer (V_D = -0.6 V) and (l) output characteristics (V_G = 0.1 to -0.7 V) of a single OECT segments module. (m) Input

voltage signals of G_1 and G_2 and corresponding output current signals of OR gates. (n) Switching performance curve of three-stage parallel OECT module on a single fiber.

EQS-IC fibers for touchless sensing

To extend functionality to wireless interaction, we developed EQS-IC fibers by integrating capacitive transmission and reception elements within a single fiber (**Fig. 5a, b**). These fibers operate in the EQS regime at 100 kHz, functioning as flexible, fully integrated, touchless sensors capable of low-frequency field generation, capacitive modulation, and near-field detection.[28] The operational principle of the EQS-IC fiber is illustrated in **Fig. 5a**. The non-shared electrode of the capacitor segment (C_S) acts as the transmitting (Tx) electrode, while the shared electrode between the C_S and R serves as the receiving (Rx) electrode. When a target object (such as a human hand) approaches, an additional capacitive coupling (C_H) forms between the target and the Rx electrode. Ground coupling via C_{TG}, C_{RG}, C_{GND}, and C_{HG} closes the circuit. Upon applying a driving signal (V_{Tx}) to the Tx electrode, the signal received at the Rx electrode (V_{Rx}) can be described as:

$$V_{Rx} = V_{Tx} \times \frac{C_S}{C_S + C_{RG} + C_H} \quad (4)$$

Equation for V_{Rx}, elaborated in **Supplementary Information**.[28] When a conductor or the human body approaches the C_S segment of the EQS-IC fiber, the value of C_H increases, resulting in a reduction of the V_{Rx}. The received voltage signal is transmitted through the R segment and collected as an output signal (V_{out}) via an oscilloscope, which digitizes the signal and relays it to a user interface (**Fig. 5c**).

A single EQS-IC fiber enables proximity-based distance measurement. By integrating data from multiple fibers (≥4), it is possible to reconstruct the three-dimensional position of a target object using a least-squares triangulation algorithm. As shown in **Fig. 5d**, four EQS-IC fibers arranged in a square configuration—each contributing a C_S segment—define an 8 × 8 cm sensing area. Real-time peak-to-peak voltage (V_{pp}) signals, which serve as proxies for object distance, are wirelessly transmitted to the user interface. These signals are used to compute and display the 3D spatial coordinates of the object on a computer in real time (see **Supplementary Fig. 21** for localization algorithm).

To minimize motion artifacts caused by hand tremors during measurement, a cardboard wrapped in aluminum foil was fixed to a holder and used as the target object. A thin copper wire connected the object to a human body, ensuring electrical continuity. To eliminate environmental noise and interference, we employed oscilloscope to extract the V_{pp} at the excitation frequency of 100 kHz as the response parameter. When a 5 V_{pp}, 100 kHz sine wave was applied to the Tx electrode of the four EQS-IC fibers, the value of V_{pp} decreased as the target object approached to the fiber, compared to the value at greater distances. The V_{pp} exhibited clear gradient changes over distances ranging from 15 cm to 1 cm (**Fig. 5e** and **Supplementary Video 3**), confirming that the EQS-IC fiber is capable of effective touchless sensing within a practical range of up to 15 cm.

Leveraging this spatial sensing capability, we implemented the EQS-IC fiber array as a touchless "remote controller," wherein finger movements within the sensing region are mapped in real time to control the spatial motion of external systems. Demonstrations include synchronized control of a virtual drone in a VR environment (**Supplementary Fig. 22** and **Supplementary Video 4**), the end effector of a robotic manipulator (**Fig. 5g**, **Supplementary Fig. 23**, and **Supplementary Video 5**), and a physical quadcopter drone (**Fig. 5h**, **Supplementary Fig. 24**, and **Supplementary Video 6**), all responding to the same gesture trajectories.

Four EQS-IC fibers are sewn parallel to two pieces of cloth. The distance between two fibers on the same piece of cloth is 1 cm. The two pieces of cloth are fixed to the inner sides of the two fingers of the robot arm, which can be used as an "automatic tracker" (**Fig. 5i**). The system continuously calculates the object's 3D coordinates by converting the V_{pp} signals from the four fibers into distance measurements. This positional data is then fed to the robotic arm's controller, enabling real-time tracking. Then the end of the robotic arm moves to the corresponding position, thereby realizing the automatic tracking of the target object by the end of the robotic arm. We conducted a simple experiment where the two-finger gripper of the robotic arm was placed horizontally (with the four fibers parallel to the ground). Holding a metal ruler in hand, we moved the ruler between the grippers and along the z-axis. The end of the robotic arm would follow the position of the ruler (**Fig. 5j** and **Supplementary Video 7**).

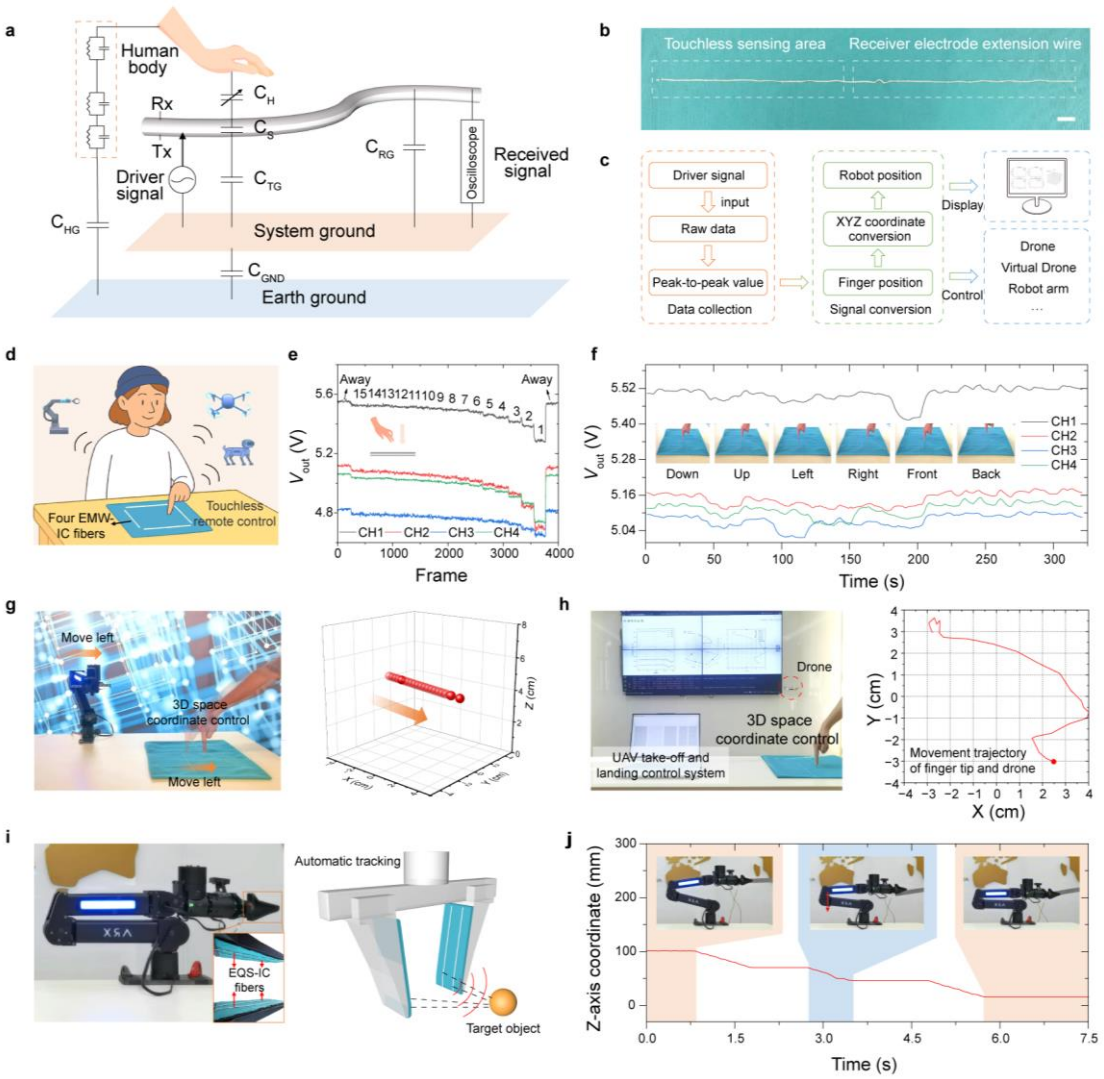


Fig. 5. EQS-IC fibers for touchless sensing. a. Schematic diagram of the mechanism for touchless sensing by EQS-IC fiber and equivalent circuit model. **b.** Photograph of EQS-IC fiber. Scale bar, 1cm. **c.** Flow chart of touchless sending and human-machine interaction using EQS-IC fibers. **d.** Schematic diagram of four EQS-IC fibers surrounded by a square as a "touchless remote controller" to control robotic arms, drones, robot dogs and other equipment. **e.** Peak voltage (100 kHz) at different distances between finger and four EQS-IC fibers. **f.** Peak voltage (100 kHz) changes of the finger moving in six directions in the touchless sensing area. Photo of using EQS-IC fibers to control the movement of the (**g**) robot arm and (**h**) drone with spatial coordinates of motion trajectory. **i.** Four EQS-IC fibers are fixed at both ends of the two-finger gripper of the robotic arm. Schematic diagram of EQS-IC fibers for robotic arm to automatically track target objects. **j.** Robotic arm target tracking images and robot arm

Z-axis coordinate change.

Conclusion

This work presents a shift in how electronic systems can be constructed, moving from fiber-on-circuit to fiber-as-circuit. Through dynamic microfluidic spinning, we encode and integrate diverse electronic functionalities—including luminescence, signal processing, logic switching, and wireless communication—into continuous, soft fiber structures. Rather than embedding chips or components into fabrics, we transform the fiber itself into a multifunctional, intelligent system. Looking forward, advances in microfluidic chip design—such as increasing the number of flow channels and reducing their cross-sectional dimensions—are expected to dramatically enhance the functional density and spatial precision of IC fibers. This strategy blurs the distinction between material and circuit, establishing fibers as the basic unit of electronic architecture and opening new frontiers for soft robotics, wearable computing, and embodied artificial intelligence.

References

1. Batra, R., Song, L. & Ramprasad, R. Emerging materials intelligence ecosystems propelled by machine learning. *Nat. Rev. Mater.* **6**, 655–678 (2021).
2. Chen, S. *et al.* Transforming Healthcare: Intelligent Wearable Sensors Empowered by Smart Materials and Artificial Intelligence. *Adv. Mater.* **37**, 2500412 (2025).
3. Turing, A. M. Computing Machinery and Intelligence. in *Parsing the Turing Test: Philosophical and Methodological Issues in the Quest for the Thinking Computer* (eds. Epstein, R., Roberts, G. & Beber, G.) 23–65 (Springer Netherlands, Dordrecht, 2009). doi:10.1007/978-1-4020-6710-5_3.
4. Cangelosi, A., Bongard, J., Fischer, M. H. & Nolfi, S. Embodied Intelligence. in *Springer Handbook of Computational Intelligence* (eds. Kacprzyk, J. & Pedrycz, W.) 697–714 (Springer, Berlin, Heidelberg, 2015). doi:10.1007/978-3-662-43505-

2_37.

5. Jiang, Y. *et al.* Highly resilient aerogel/sponge nested structures assisted multimodal tactile sensory system for robotic embodied perception. *Nano Energy* **131**, 110279 (2024).
6. Chen, S. *et al.* Exploring Embodied Multimodal Large Models: Development, datasets, and future directions. *Inf. Fusion* **122**, 103198 (2025).
7. Mengaldo, G. *et al.* A concise guide to modelling the physics of embodied intelligence in soft robotics. *Nat. Rev. Phys.* **4**, 595–610 (2022).
8. Choi, H. W. *et al.* Smart textile lighting/display system with multifunctional fibre devices for large scale smart home and IoT applications. *Nat. Commun.* **13**, 814 (2022).
9. Ma, X. *et al.* A monolithically integrated in-textile wristband for wireless epidermal biosensing. *Sci. Adv.* **9**, eadj2763 (2023).
10. Yang, Y. *et al.* A non-printed integrated-circuit textile for wireless theranostics. *Nat. Commun.* **12**, 4876 (2021).
11. Choi, K.-H. *et al.* Fibriform Organic Electrochemical Diodes with Rectifying, Complementary Logic and Transient Voltage Suppression Functions for Wearable E-Textile Embedded Circuits. *ACS Nano* **17**, 5821–5833 (2023).
12. Shi, X. *et al.* Large-area display textiles integrated with functional systems. *Nature* **591**, 240–245 (2021).
13. Gupta, N. *et al.* A single-fibre computer enables textile networks and distributed inference. *Nature* **639**, 79–86 (2025).

14. Rein, M. *et al.* Diode fibres for fabric-based optical communications. *Nature* **560**, 214–218 (2018).
15. Loke, G. *et al.* Digital electronics in fibres enable fabric-based machine-learning inference. *Nat. Commun.* **12**, 3317 (2021).
16. Hwang, S. *et al.* Integration of multiple electronic components on a microfibre towards an emerging electronic textile platform. *Nat. Commun.* **13**, 3173 (2022).
17. Zhong, Y. *et al.* High-Performance Fiber-Shaped Vertical Organic Electrochemical Transistors Patterned by Surface Photolithography. *Chem. Mater.* **35**, 9739–9746 (2023).
18. Sun, F. *et al.* Soft Fiber Electronics Based on Semiconducting Polymer. *Chem. Rev.* **123**, 4693–4763 (2023).
19. Ma, J. *et al.* Axially Encoded Mechano-Metafiber Electronics by Local Strain Engineering. *Adv. Mater.* **35**, 2305615 (2023).
20. Ma, J., Liu, Y., Gao, C. & Xu, Z. Sequence spinning axially encoded metafibers. *Matter* **6**, 3940–3955 (2023).
21. Kang, E. *et al.* Digitally tunable physicochemical coding of material composition and topography in continuous microfibres. *Nat. Mater.* **10**, 877–883 (2011).
22. Li, G. *et al.* Autonomous Electroluminescent Textile for Visual Interaction and Environmental Warning. *Nano Lett.* **23**, 8436–8444 (2023).
23. Sun, F. *et al.* Stretchable Conductive Fibers of Ultrahigh Tensile Strain and Stable Conductance Enabled by a Worm-Shaped Graphene Microlayer. *Nano Lett.* **19**, 6592–6599 (2019).

24. Wang, X. *et al.* Ultrastable N-Type Semiconducting Fiber Organic Electrochemical Transistors for Highly Sensitive Biosensors. *Adv. Mater.* **36**, 2400287 (2024).
25. Yang, W. *et al.* Single body-coupled fiber enables chipless textile electronics. *Science* **384**, 74–81 (2024).
26. Huysmans, M. & Dassargues, A. Review of the use of Péclet numbers to determine the relative importance of advection and diffusion in low permeability environments. *Hydrogeol. J.* **13**, 895–904 (2005).
27. Jiang, H. *et al.* Shear-enhanced liquid crystal spinning of conjugated polymer fibers. *Natl. Sci. Rev.* nwaf331 (2025) doi:10.1093/nsr/nwaf331.
28. Zhou, J. *et al.* Mormyroidea-inspired electronic skin for active non-contact three-dimensional tracking and sensing. *Nat. Commun.* **15**, 9875 (2024).

Methods

Design and 3D printing of microfluidic chip

In this study, we designed a five-channel microfluidic chip. The microfluidic chip model (**Supplementary Fig. 2**) was initially designed using Solidworks software. The model was subsequently printed using an SLA 3D printer (Form 3B+). Prior to printing, the model file was imported into the printer's software (PreForm) for preprocessing. Key parameters were configured, including a layer thickness of 0.025 mm and the generation of a comprehensive base support, with support contact points set to 0.4 mm in size. Following these settings, the processed model was transferred to the 3D printer for fabrication. Upon completion of the printing process, the printed chip was washed in anhydrous ethanol for 20 min to effectively remove any residual photopolymer resin (Clear V4, FORMLABS Inc., America).

Programmable fluid control system for microfluidic spinning

The microfluidic spinning system consists of four primary components: the liquid reservoir, control module, microfluidic chip, and coagulation bath. The liquid reservoirs (15 ml) are aligned with the number of inlets on the microfluidic chip, supplying the required spinning solutions to each corresponding channel. A high-precision pneumatic pump (Flow EZ, Range:7000 mbar, **Supplementary Fig. 1b**) independently controls the fluid pressure and flow rate in each channel. A high-precision pneumatic pump is utilized to independently regulate the fluid pressure and flow rate of the spinning solutions in different channels. For channels using the same spinning solution, a pressure switch (P-Switch, Range:2000 mbar, **Supplementary Fig. 1b**) can also be employed for unified control. The P-Switch features two input ports, which can be connected to two pneumatic pumps (designated as Flow EZ #1 and Flow EZ #2), and eight output ports that can toggle between controlling the output pressure from either Flow EZ #1 and Flow EZ #2. Centralized control and programming of both the high-precision pneumatic pump and the P-Switch are achieved through the microfluidic system software (Fluigent OxyGEN, **Supplementary Fig. 1c, d**). This setup enables

precise control over the flow and stoppage of fluids in each channel, thereby allowing simultaneous axial and radial (spatial) encoding. Once encoded, the spinning solution flows through the microfluidic chip into the coagulation bath, where it rapidly solidifies, preserving the encoded sequence and yielding spatially encoded fibers.

Spatially encoded microfluidic spinning technique

All materials including Thermoplastic polyurethane (TPU, Bayer 385S, Dongguan Zhonghui Plastic New Materials Co., Ltd., China); Red, yellow, green, blue and purple pigments (MT Series, average particle size ⩽ 6 μm, Shanghai Haoshijia Building Materials Supermarket, China); ZnS:Cu^{2+} phosphor (D502CT, 25 μm, CAS number: 68611-70-1, Shanghai Keyan Phosphor Technology, China); $BaTiO_3$ (100 nm, Quanzhou Qi Jin New Material Co., Ltd., China); Silver paste (01L-2211D, Shenzhen Sryeo Lectronic Paste Co., Ltd., China); Poly[3,3′-bis[2-[2-(2-methoxyethoxy)ethoxy]ethoxy]-2,2′:5′,2″-terthiophene-5,5″-diyl] (p(g2T-T), CAS number: 1974310-62-7, made by the laboratory); 1-Ethyl-3-Methylimidazolium bis(triFluoroMethylSulfonyl)Imide ([EMIM][TFSI], CAS number: 174899-82-2, Shanghai Haohong Biopharmaceutical Technology Co., Ltd., China); N,N-Dimethylformamide (DMF, Shanghai Titan Technology Co., Ltd., China); Deionized water (made by the laboratory) were commercially available and used as received.

We employed a 25 wt% TPU spinning solution with DMF as the solvent and the deionized water as coagulation bath to explore the spatially encoded microfluidic spinning technique. Five equal portions of the 25 wt% TPU solution were prepared, and each was mixed with equal masses of red, orange, green, blue, and purple pigment, respectively, at a pigment-to-TPU solution mass ratio of 1:10. The spinning process was carried out using a microfluidic chip with five input channels, where the outlets (600 × 600 μm) of the chip were immersed in the coagulation bath.

The five colored spinning solutions were individually connected to the five-channel chip, and pneumatic pressure was supplied through outputs ①, ②, ③, ④, and ⑤ of the P-Switch. The two input ports of the P-Switch were connected to Flow EZ #1 and Flow EZ #2, respectively. Flow EZ #1 is set to a pressure of 1500 mbar to drive the

fluid flow, while Flow EZ #2 is maintained at 10 mbar to prevent backflow of the stationary fluid. The desired spatially encoded fiber structure is first designed, followed by programming the fluid flow in the five channels using microfluidic software to achieve the specified fiber architecture. The microfluidic software supports a minimum fluid switching time interval of 0.001 ms. To ensure the integrity of the encoded fiber structure, we set the fluid switching time interval (resolution) for this chip at the given pressure to ≥1 s. Notably, the smaller the channel dimensions of the chip, the shorter the achievable fluid switching time at the same flow rate, resulting in a higher resolution of the encoded fiber structure. We performed independent spinning based on two major structural types: one maintaining a consistent total number of layers for the switching of the five colors within the fiber, and the other maintaining uniform time intervals for the switching of the five colors (**Supplementary Fig. 5**). Finally, these two structural types were integrated into a single fiber.

Conductive layer spinning solution. A 25 wt% TPU solution was prepared using DMF as the solvent. Conductive silver paste was added to the TPU solution at a mass ratio of 2:1, which was determined as the optimal ratio based on sheet resistance and film-forming properties. The mixture was stirred thoroughly to obtain a homogeneous conductive layer spinning solution.

luminescent layer spinning solutions. A 25 wt% TPU solution was prepared using DMF as the solvent. Red, green, and blue fluorescent pigments were then added to the TPU solution at a mass ratio of 1:5, followed by thorough stirring to obtain uniform RGB TPU solutions. Commercial ZnS:Cu phosphor powder was subsequently dispersed into each of the prepared RGB TPU solutions at a mass ratio of 1:1, resulting in the final luminescent layer spinning solutions for the RGB primary colors.

Insulating layer spinning solution. A 25 wt% TPU solution was prepared using DMF as the solvent. $BaTiO_3$ was added to the TPU solution at a mass ratio of 1:5, followed by thorough stirring to obtain a homogeneous insulating layer spinning solution.

Semiconductor layer spinning solution. A 25 wt% TPU solution was prepared using DMF as the solvent. P(g2T-T) dissolved in DMSO at a concentration of 7.5 mg mL^{-1} was mixed with p(g2T-T) dissolved in 25% TPU at 2 mg mL^{-1} in a volume ratio of 2:1,

followed by thorough stirring to obtain a homogeneous semiconductor layer spinning solution.

Fabrication process of EL-IC fibers. Using the five-channel chip, the spinning solutions in channels #1, #2, #3, #4, and #5 were sequentially loaded with the conductive spinning solution, R, G, and B luminescent spinning solutions, and another conductive spinning solution. The fluid encoding sequence of this fiber is illustrated in **Fig. 3a, d**.

Fabrication process of RC-IC fibers and EQS-IC fibers. Using the five-channel chip, the solutions in channel #1 loaded with the conductive spinning solution, channel #2, #3, and #4 loaded with insulating spinning solutions, and channel #5 loaded with another conductive spinning solution. The fluid encoding sequence of RC-IC fibers and EQS-IC fibers are illustrated in **Fig. 4a, e**.

Fabrication process of OECT-IC fibers. Using the five-channel chip, the spinning solutions in channels #1, #2, #3, #4, and #5 were sequentially loaded with the conductive spinning solution, insulating spinning solutions, conductive spinning solution, semiconductor spinning solution, and another conductive spinning solution. The fluid encoding sequence of this fiber is illustrated in **Figure 4i**.

Derivation formula of the Péclet number for diffusion between adjacent fluid layers[26]

Assuming the flow velocity of all five solutions is the same, the *Pe* between each adjacent solution layer i and j can be expressed as:

$$Pe_{ij} = vw_{ij}/D_{ij} \tag{5}$$

where w_{ij} is the width of the adjacent solution layer (m), D_{ij} is the diffusion coefficient of the adjacent solution layer ($m^2\ s^{-1}$), and v is the average flow velocity (m s^{-1}). Since the flow direction of the spinning solution is orthogonal to the diffusion direction, the two processes can be analyzed independently. Therefore, the *Pe* can be expressed as:

$$Pe_{ij} = l_{ij}/w_{ij} \tag{6}$$

549 The distance l_{ij} travelled by the fluid before diffusion spans the entire adjacent
550 solution layer can be calculated as:

551 $$l_{ij} = vw_{ij}^2/D_{ij} \quad (7)$$

552 ## Characterization and measurement

553 Field emission scanning electron microscopy (SEM MERLIN, Carl Zeiss), confocal
554 laser scanning microscopy (Leica TCS SP5II) was used to characterize the microscopic
555 morphology of the fibers. Optical photos and demonstration videos were taken by a
556 digital camera (Sony A7C1). Mechanical properties of the fibers were tested by
557 electronic universal testing machine (Instron 5969). The resistance and capacitance of
558 the fiber are tested with the high-precision digital multimeter (Keithley DMM6500).
559 The electrical characteristics of the OECT were tested under ambient conditions using
560 a source meter (Keithley 2450). The input waveform of RC-IC and EQS-IC fibers were
561 generated by a function generator (Tektronix AFG31000). The electrical properties of
562 RC-IC and EQS-IC fibers were tested with the oscilloscope (Tektronix MSO44). The
563 application demonstrations use ARX GF100 robotic arm and DJI Tello drone.

564 ## Microfluidic spinning simulation

565 Three-dimensional computational fluid dynamics (CFD) simulations were performed
566 using ANSYS Fluent 2023 R1 to investigate the structural formation, interface diffusion
567 and dynamic flow coding in the microfluidic wet spinning process. The 3D model of
568 the microfluidic chip was constructed in SolidWorks based on the actual device
569 dimensions (see **Supplementary Fig. 2**), including five symmetric inlet branches
570 merging into a common outlet channel. The full geometry was imported into ANSYS
571 Fluent via meshing in ANSYS Meshing with tetrahedral elements, and refined near
572 junction zones to resolve interface deformation. Mesh independence was verified by
573 comparing velocity profiles and volume fraction convergence.

574 To accurately represent the rheological behavior of the spinning dopes, each inlet
575 fluid was defined using the Carreau non-Newtonian viscosity model.[29] Material
576 viscosity parametersfor each flow (channels A-E) were experimentally measured in

Supplementary Fig. 8.

The inlet boundary conditions were defined as velocity inlets with controlled magnitudes (0 or 0.005 m s^{-1}), corresponding to different encoding states. The outlet was set as pressure-outlet at 0 Pa. The simulation was performed under steady-state, laminar, multiphase (VOF) settings, with surface tension neglected due to high Péclet numbers. Interface resolution was ensured using a geometric reconstruction scheme and a volume fraction cutoff of 10^{-6}.

Seven flow encoding patterns (states 1–7) were simulated (**Fig. 2e**), each corresponding to a different RGB combination. For each state, the simulation solved the velocity field, pressure distribution, and volume fraction of each phase. The output included cross-sectional profiles and streamline plots at key downstream locations.

Electromagnetic simulation

The finite element analysis (FEA) was conducted using the commercial electromagnetic simulation software Ansys HFSS 15.0, where a tetrahedral mesh and adaptive meshing strategy were applied to ensure numerical convergence. Radiation boundaries were applied at the outer domain as numerical open boundaries, preventing spurious reflections without implying actual far-field radiation. The fiber structure was modeled as a straight cylindrical conductor with a diameter of 1 mm, and a capacitive segment length of 80 mm, the total length of the EQS-IC fiber is 160 mm. The ground reference (port2) was placed at a distance of 260 mm from the signal excitation point. A sinusoidal voltage source with an amplitude of 5 V and frequency of 100 kHz was applied at the Tx electrode to emulate the signal emission process. A metallic rod (d = 10 mm) representing a human finger was introduced into the simulation as a grounded conductor. The plate was placed at a horizontal position of 120 mm and a vertical height ranging from 10 mm to 100 mm above the fiber, in order to evaluate capacitive coupling strength and spatial response sensitivity. The wavelength corresponding to the driving frequency was set to ~3 km, and parametric sweeps were performed to analyze the change in electric potential at the Rx electrode under different proximity conditions.

Data availability

All data are contained within the manuscript. Raw data are available from the corresponding authors upon reasonable request.

Code availability

Custom code used in this study is available from the corresponding authors upon reasonable request.

29. Wu, C., Almuaalemi, H. Y. M., Sohan, A. S. M. M. F. & Yin, B. Effect of Flow Velocity on Laminar Flow in Microfluidic Chips. *Micromachines* **14**, 1277 (2023).

ACKNOWLEDGMENTS

Funding

This research is supported by the Key R&D Program of Shandong Province, China (2024CXGC010411), the Fundamental Research Funds for the Central Universities (2232025A-06, 2232024Y-01, CUSF-DH-D-2024001), DHU Distinguished Young Professor Program (LZB2025002), the National Natural Science Foundation of China (52373282, 52173156, 52273316), the Science and Technology Commission of Shanghai Municipality (23ZR1402000, 24520713100), the Taishan Industrial Experts Programme Special Funding (NO.tscx202408117), the Pujiang Project of the Shanghai Magnolia Talent Program (No.24PJD001), the Sichuan Science and Technology Program (Grant Nos. 2022NSFSC0877).

Author contributions

Authors and Affiliations

State Key Laboratory of Advanced Fiber Materials, Donghua University, Shanghai, China.

Fenggiang Sun, Fen Jiang, Kaige Wang, Weichu Chen, Yida Hong, Xingbo Han, Yuwen Zhu, Hengda Sun, Hongzhi Wang, Meifang Zhu & Gang·Wang

College of Materials Science and Engineering, Donghua University, Shanghai, China.

Fenggiang Sun, Fen Jiang, Kaige Wang, Weichu Chen, Yida Hong, Xingbo Han, Yuwen Zhu, Hengda Sun, Hongzhi Wang, Meifang Zhu & Gang·Wang

College of Information Science and Technology, Donghua University, Shanghai, China

Futeng Zhu, Mingbo Zhao

Contributions

F.S., Y.Z., H.S., and G.W. conceived the idea and designed the experiments. F.J., K.W., and F.S. conducted the fabrication and testing of EL-IC, RC-IC, and EQS-IC fibers. K.W., Y.H., and F.S. conducted material characterization experiments. W.C. conducted the fabrication and testing of OECT-IC fibers. X.H. conducted the fluid simulation. F.L. conducted the algorithm and code. F.L. and F.S. conducted the robot experiments. All authors discussed and analysed the data. F.S. prepared the manuscript with inputs from all other co-authors.

Corresponding authors

Correspondence to Hengda Sun or Gang Wang.

Competing interests

The authors declare that they have no competing interests.

Additional information

Supplementary Information is available for this paper.

Supplementary Files

This is a list of supplementary files associated with this preprint. Click to download.

- SupplementaryMaterials.docx
- SupplementaryVideo1.mp4
- SupplementaryVideo2.mp4
- SupplementaryVideo3.mp4
- SupplementaryVideo4.mp4
- SupplementaryVideo5.mp4
- SupplementaryVideo6.mp4
- SupplementaryVideo7.mp4